

# Amine-Terminated Carbon Dots Linking Hole Transport Layer and Vertically Oriented Quasi-2D Perovskites through Hydrogen Bonds Enable Efficient LEDs

Wei Dong, Xiaoyu Zhang,\* Fan Yang, Qingsen Zeng, Wenxu Yin, Wei Zhang, Haoran Wang, Xuyong Yang, Stephen V. Kershaw, Bai Yang, Andrey L. Rogach,\* and Weitao Zheng\*



Cite This: *ACS Nano* 2022, 16, 9679–9690



Read Online

ACCESS |

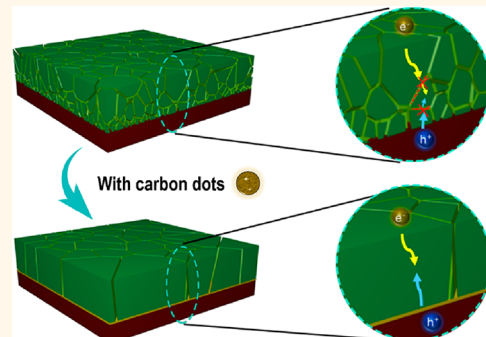
Metrics & More

Article Recommendations

Supporting Information

**ABSTRACT:** Close attention to the interfaces of solution-processed metal halide perovskite-based light-emitting devices (LEDs) is crucial for their optimal performance. Solution processing of these devices typically leads to the formation of van der Waals interfaces with a weak connection between different functional layers, leaving great room for improvement in charge transport through strengthening of the interlayer interaction. Here, we have realized a hydrogen-bond-assisted interface that makes use of ultrasmall amine-terminated carbon dots to enhance the interaction between the hole transport layer made of PEDOT:PSS and the hybrid lead bromide perovskite emitting layer, which not only promotes the hole injection efficiency but also orients the quasi-2D perovskite crystals penetrating the vertical direction of the device without any, or very few, horizontal grain boundaries, which has a profound effect on the photophysical and transport properties of the emitting layer. As a result, LEDs based on quasi-2D perovskites show up to 24.5% external quantum efficiency, 80 000 cd m<sup>-2</sup> brightness, and over 5-fold extended longevity.

**KEYWORDS:** quasi-2D perovskites, light-emitting device, carbon dots, interface, hydrogen bonds



Effect-tolerant lead halide perovskites combine tunability of their semiconductor energy bandgaps with low-cost solution processing;<sup>1–4</sup> they serve as a light harvester in solar cells and as an emitter in light-emitting devices (LEDs),<sup>5–8</sup> with a large degree of control of the carrier lifetime and diffusion length.<sup>9–15</sup> Quasi-two-dimensional (Q-2D) perovskites are quantum-confined materials along their out-of-plane direction, which ideally should be grain-boundary-free in-plane.<sup>16,17</sup> As such, strong emission of these materials could be facilitated by realizing a favorable balance between carrier transport and exciton formation, providing the basis for efficient electroluminescence (EL) in LEDs. Based on these advantages, Q-2D perovskite-based LEDs have seen great progress in recent years<sup>18–24</sup> since the demonstration of the first visible<sup>24</sup> and near-infrared<sup>16</sup> Q-2D perovskite LEDs. For butylamine (BA)-based Q-2D lead halide perovskites, oriented crystal growth parallel to the substrate is common as a result of minimizing the surface energy (the BA-terminated planes have the lowest surface energy),<sup>25</sup> which requires carrier tunneling or hopping between adjacent crystals during the LED

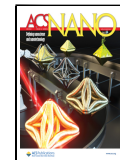
operation. However, in these crystals adjacent inorganic perovskite units are typically separated by low-conductivity organic spacing layers, which greatly hinders the charge transport. Therefore, vertically oriented growth of Q-2D perovskites forming emitting layers is more desirable for efficient radiative transitions in such LEDs; however to date this has rarely been reported.

Solution-processed perovskite films possess several advantages such as an ease of manufacturing and high fabrication throughput; however they typically show insufficient adhesion to substrates. In heterostructures composed of Q-2D perovskites and organic hole/electron transporting layers, there is often a van der Waals gap, which leads to a carrier tunneling

Received: March 28, 2022

Accepted: June 1, 2022

Published: June 5, 2022



ACS Publications

© 2022 American Chemical Society

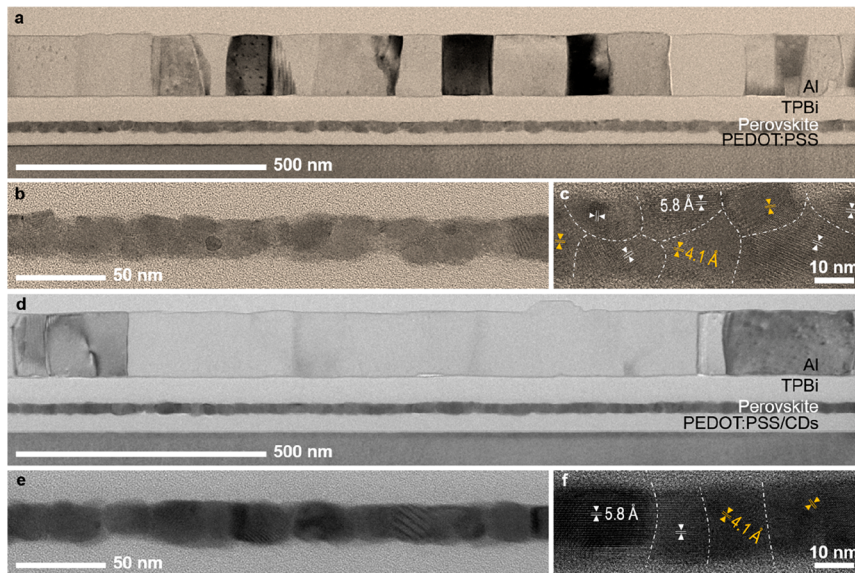


**Figure 1. Direct observation of the Q-2D perovskite LEDs using FIB combined with TEM.** Cross-section TEM images of Q-2D perovskite LEDs without (a, b, and c) and with (d, e, and f) CDs. The same-colored arrows stand for the same crystal planes: white and yellow arrows correspond to (100) and (110) crystal planes of perovskites, respectively.

barrier and increases the injection resistance. Such van der Waals gaps are inevitable in 2D materials such as graphene, MoS<sub>2</sub>, WS<sub>2</sub>, ReS<sub>2</sub>, ZrS<sub>2</sub>, InSe, GaSe, and black phosphorus and optoelectronic devices based thereon,<sup>26</sup> this has been identified as a major source of the tunneling barrier able to block the charge transport.<sup>27</sup>

Here, we eliminate the van der Waals gap by linking the Ba<sub>2</sub>Cs<sub>n-1</sub>Pb<sub>n</sub>Br<sub>3n+1</sub> Q-2D perovskite serving as an emitting layer with a poly(3,4-ethylenedioxythiophene):poly(styrenesulfonate) (PEDOT:PSS) hole-transporting layer (HTL) *via* hydrogen bonds, using ultrasmall ( $\sim 2$  nm) amine-terminated carbon dots (CDs). On one hand, the CDs serve as anchored nucleation centers inducing preferential crystallization and thus leading to vertically oriented growth of penetrating Q-2D perovskites, which smooths the energy transfer pathway and enhances the EL efficiency of the resulting LEDs. On the other hand, CDs compete with PEDOT (conductive component) in bonding with the PSS (an insulating surfactant), leading to a PEDOT-rich surface of the HTL, which increases the carrier mobilities and decreases the surface potential, and thus promotes the hole injection into emitting layer of LEDs. The use of ultrasmall  $\sim 2$  nm CDs results in a compact film enabling efficient charge transfer between the HTL and emitting layer. By comparing the device performance of LEDs with and without CDs, we demonstrate multiple benefits of the hydrogen bond assisted interfaces, which improve charge transport and thus the device brightness and EL efficiency, enabling a record high peak external quantum efficiency (EQE) of 24.5%, combined with 80 086 cd m<sup>-2</sup> brightness and over 5-fold extended longevity of LEDs.

## RESULTS

In Figure S1 (Supporting Information), we depict the construction of Q-2D perovskite films. PEDOT:PSS was spin-coated on patterned indium tin oxide (ITO) glass substrates and annealed at 150 °C for 15 min in air. CDs in a 2-methoxyethanol solution with an appropriate concentration ( $\sim 0.04$  mg mL<sup>-1</sup>) were spin-coated on the PEDOT:PSS HTL and annealed at 130 °C for 5 min. Then, the substrates were

transferred into a N<sub>2</sub>-filled glovebox for further processing. The perovskite precursor solution consisting of butylammonium bromide (BABr), cesium bromide (CsBr), lead bromide (PbBr<sub>2</sub>), poly(ethylene oxide) (PEO), and dimethyl sulfoxide (DMSO) (see Methods for details) was spin-coated on ITO/HTL or ITO/HTL/CDs substrates, followed by thermal annealing. Figure S2 in the Supporting Information shows a typical transmission electron microscopy (TEM) image of the CDs employed here, which are rather monodisperse spherical-shaped particles with a diameter of  $\sim 2$  nm. Fourier transform infrared (FTIR) spectra of CDs presented in Figure S3a (Supporting Information) show the presence of -CH, C=C, C=O, and -NH<sub>2</sub> surface functional groups, with the amine groups being dominant at the surface of CDs. A UV-vis absorption spectrum of the CDs is shown in Figure S3b (Supporting Information) alongside a photoluminescence (PL) spectrum of the Ba<sub>2</sub>Cs<sub>n-1</sub>Pb<sub>n</sub>Br<sub>3n+1</sub> Q-2D perovskites; there is no overlap between them, indicating that introducing CDs into LEDs would not influence the light extraction from the perovskite.

According to the literature, PbBr<sub>2</sub>-DMSO, PbBr<sub>2</sub>-2DMSO, and/or Cs<sub>2</sub>Pb<sub>3</sub>Br<sub>8</sub>-2DMSO intermediates form first and then react with CsBr to convert into perovskites.<sup>28</sup> For the case of the ITO/HTL substrate, nucleation starts from the liquid surface as a result of solvent evaporation,<sup>29,30</sup> followed by a downward growth of the Q-2D perovskites, which leads to a nonoriented film with the formation of tiered crystals (Figure S4a in the Supporting Information). This is due to the fact that, when the upper layer crystals end their growth and are capped by BA<sup>+</sup> and PEO, beneath them a lower layer still consists of intermediates with DMSO molecules. Thus, the precursors cannot be completely converted into perovskite in a single stage, and complete conversion does not occur until subsequent annealing, which results in nonoriented films with a lot of grain boundaries. For the case of the ITO/HTL/CDs substrate, the presence of CDs with plenty of -NH<sub>2</sub> groups at the surface leads to interactions with intermediates from the precursor solution;<sup>31</sup> this allows the formation of multiple nucleation centers at the bottom part of the precursor solution,

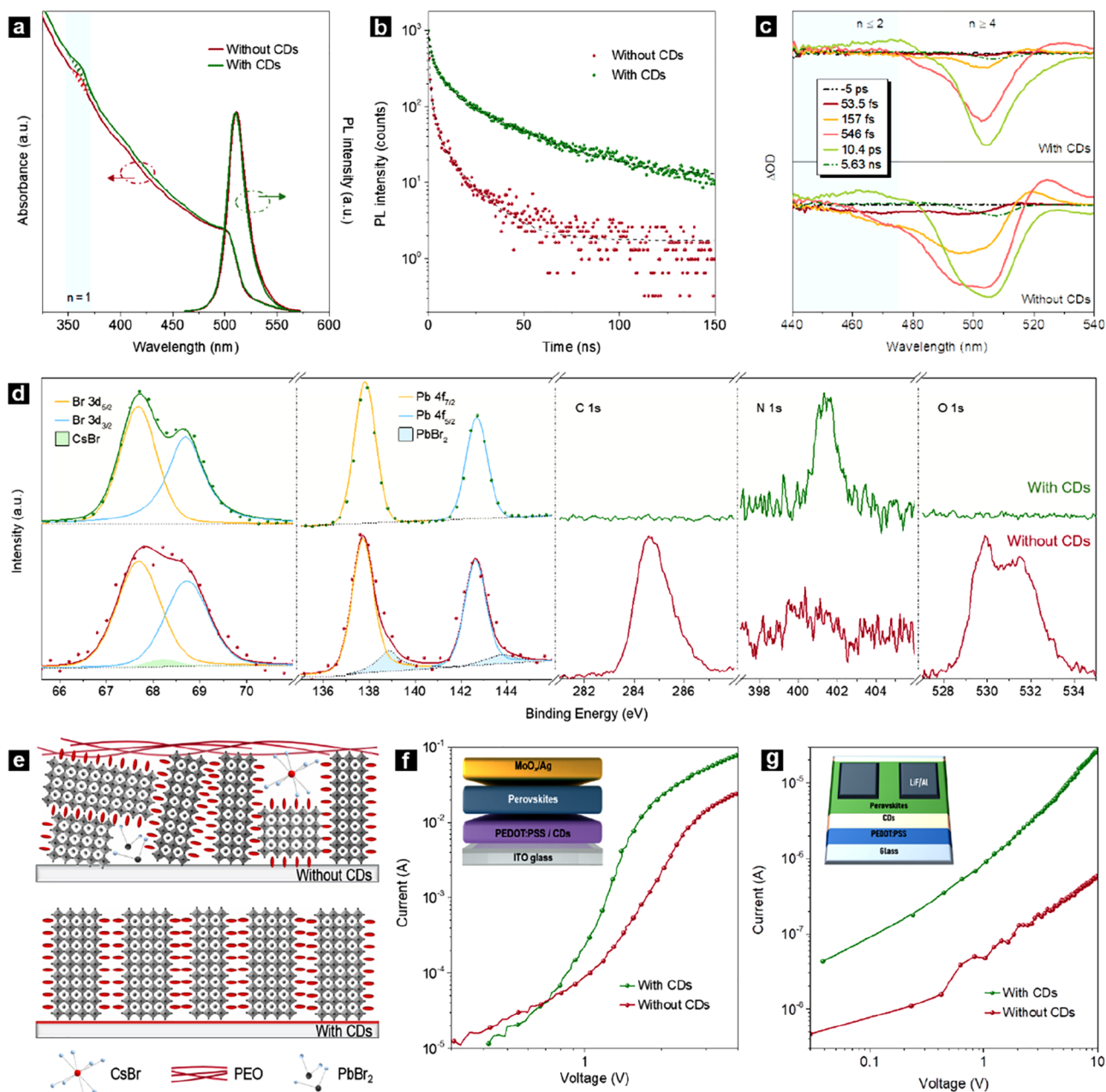


**Figure 2.** Basic properties of Q-2D perovskite films. (a) UV-vis absorption and PL spectra, (b) PL decays, and (c) TA spectra at selected probe decay times of Q-2D films on PEDOT:PSS, with and without CDs. The excitation and emission wavelengths of PL decays are 400 and 510 nm, respectively. The pump wavelength of TA characterization is 420 nm. (d) XPS spectra of PEDOT:PSS/CDs/perovskite (green) and PEDOT:PSS/perovskite (red) films for Br 3d, Pb 4f, C 1s, N 1s, and O 1s elements. (e) Schematic diagram of the structures of Q-2D perovskite films with and without CDs on a PEDOT:PSS surface. (f) Current–voltage curves of the “hole-only” devices (with the respective structure provided in an inset), with and without CD interlayers. (g) Current–voltage curves of the lateral structured devices testing the surface electron conductivity of Q-2D perovskites with and without a CD interlayer. The employed device structure is shown as an inset: both PEDOT:PSS film and perovskite film have thicknesses of ~30 nm; CD film consists of approximately one monolayer (~2 nm); thicknesses of Ag and Al electrodes are ~100 nm; thicknesses of MoO<sub>x</sub> and LiF layers are ~1 nm; the electrode separation distance is ~80  $\mu$ m.

as well, which is followed by growth of perovskite crystals from the top and from the bottom toward the middle of the film, resulting in the out-of-plane oriented growth (Figure S4b in the Supporting Information).<sup>32</sup> With a suitable growth rate and appropriate heat treatment (see Methods for details), perovskite crystals formed at the top and the bottom can fuse together, leading to the formation of vertically oriented, penetrating crystals without, or with very few, horizontal grain boundaries. As illustrated in Figure S5a (Supporting

Information), a nonoriented film with plenty of small grains and multiple horizontal grain boundaries suffers from a severe degree of nonradiative recombination,<sup>16,17,33</sup> which is harmful to the EL performance of LEDs. On the contrary, a Q-2D perovskite film formed with the assistance of CDs with vertically oriented crystals without significant numbers of horizontal grain boundaries can avoid the negative effect on charge transport caused by the low-conductivity organic spacing layers that are necessarily present at the grain

boundaries (Figure S5b in the Supporting Information). Thus, due to the regulating effect of the CDs on the crystallization kinetics, the perovskite films change their morphology from multilayered crystals to single-layer, more uniform crystals, which significantly inhibits the quenching of carriers at boundaries, as will be demonstrated below.

The orientation of the Q-2D perovskite films is directly observed by using the focused ion beam (FIB) technique combined with TEM. LEDs with the structure of anode/PEDOT:PSS/CDs/Q-2D perovskite/TPBi/LiF/Al were used for TEM sample preparation (TPBi is 1,3,5-tris(N-phenylbenzimidazol-2-yl)benzene). As shown in Figure 1a and d, the perovskite film thicknesses are ~30 nm in both cases; however their grain size and crystal orientation vary greatly. For the sample without CDs, the Q-2D perovskite film consists of at least two layers of irregularly shaped crystals, and the crystal orientation is disordered (Figure 1a and b). For the CD-assisted sample on the contrary, the perovskite film consists of a layer of quasi-square crystals, and all of the crystals have an edge parallel or nearly parallel to the substrate (Figure 1d and e). Lattice spacings of 0.58 and 0.41 nm are measured from the high-resolution TEM (HRTEM) images for both control (without CDs) and CD-assisted samples (Figure 1c and f), which correspond to the (100) and (110) interplanar spacings, respectively, demonstrating that crystals observed in the TEM images are indeed oriented perovskites.

We further distinguished the perovskite crystal and grain boundaries by comparative analysis of the bright field, dark field, and high-angle annular dark field (HAADF) images of the same area (Figure S6 in the Supporting Information). In the bright field images, the lead-containing domains appear to be darker, while the light elements containing organic spacers are difficult to distinguish due to the lower electron-scattering cross section. In the dark field images on the other hand, the lead-containing domains appear to be lighter, while the organic spacers tend to appear as darker phases. HAADF as an extension of dark field imaging provides more proportional correlation between color depth and element weight. Clearly, the Q-2D perovskite films grown without CDs are composed of fine crystals and accompanied by a large number of grain boundaries, while that of the CD-assisted films are monolayers of upright quasi-rectangular crystals.

We further deepened our understanding of how the CDs make the Q-2D perovskite films denser by analyzing the X-ray diffraction (XRD) data. The XRD patterns are given in Figure S7 (Supporting Information), showing two peaks at 13.9° and 16.8°, which are attributed to the  $n = 4$  and  $n = 1$  phases,<sup>34,35</sup> respectively, suggesting a thermodynamically favored<sup>36</sup> phase distribution dominated by  $n = 4$  and  $n = 1$  phases. Given that Q-2D perovskites are often an ensemble of self-organized multiple-quantum wells with a phase distribution ranging from  $n = 1$  to  $n = \infty$ , the unobservable phases in XRD patterns like  $n = 2$  and  $n = 3$  phases may be as a result of their limited content and/or long-range disorder. The coexistence of other  $n$  phases in the samples under study is revealed by the distinguishable energy transfer signals from the transient absorption dynamics, as will be discussed in relation to Figure 2c. We roughly estimated the proportion of each phase in the perovskite film by calculating the XRD peak intensity ratio of  $n = 4$  to  $n = 1$  phases, which we denote as  $R_{4/1}$ . The  $R_{4/1}$  value of the sample without CDs is 2.1 and increases to 3.5 after introducing the CDs. Since CDs do not change the perovskite film thickness, and the  $n = 4$  phase is much thicker than the  $n = 1$  phases, for a

given area (like the X-ray spot size), a larger  $R_{4/1}$  means fewer crystals and fewer grain boundaries, that is to say, a denser film. To better understand how CDs affect perovskite crystallization, we carried out the grazing incidence wide-angle X-ray scattering (GIWAXS) measurements on perovskite films with or without CDs. As shown in Figure S8 in the Supporting Information, GIWAXS patterns indicate that both kinds of perovskite films have a preferential edge-on orientation relative to the substrates. The film with CDs shows better pronounced Bragg spots as compared with film without CDs, which confirms its more regular orientation (see schematics depicted in Figure S8 on the right), which is consistent with the TEM characterization results. Moreover, the former film exhibits more intense GIWAXS patterns, which is due to its better crystallinity as compared with the film without CDs. The CD-assisted perovskite film with more regular orientation and higher crystallinity can achieve more efficient charge transport.

The change in Q-2D perovskite crystal orientation and reduction in the number of grain boundaries while using CDs offers a means to optimize their properties. As shown in Figure 2a, the absorption spectra normalized at the absorption peak (500 nm) of samples with or without CDs have similar shapes and exhibit small peaks at ~410 nm (corresponding to the  $n = 1$  phase). In the short-wavelength region below 500 nm, the HTL/CDs/perovskite sample has stronger light absorption than the HTL/perovskite sample. Since TEM results have shown that CDs did not influence the thickness of the perovskite film, the enhanced light absorption points out that CDs have induced closer packing of the perovskite crystals, which is in line with the reduced number of grain boundaries. The absorption of CDs is next to nothing when the wavelength is longer than ~420 nm, while the absorption of perovskites is fully enhanced in the wavelength range shorter than ~500 nm; we thus infer that the ultrathin CD film has no or little effect on absorption enhancement. Besides, as shown in the GIWAXS patterns in Figure S8 in the Supporting Information, the Debye–Scherer ring of the (040) plane belonging to the  $n = 1$  phase appears after the introduction of CDs. The  $n = 1$  phase can also be identified in the absorption spectra of both kinds of perovskite films, indicating that it exists as periodic and nonperiodic phases incorporated within the perovskite films with and without CDs, respectively.

In Q-2D perovskites, energy transfer between different  $n$  phases is a preferentially downhill process, where low- $n$  phases serve as donors because of their larger bandgaps and high- $n$  phases serve as acceptors due to their relatively smaller bandgaps. Based on our previous study,<sup>33</sup> increasing the acceptor-to-donor ratio will enhance the energy transfer from the donor to acceptor in the perovskite films, thereby improving their light emission efficiency. The energy transfer process was studied by combination of steady-state PL, time-resolved photoluminescence spectroscopy, and transient absorption (TA) spectroscopy. The PL peak slightly blueshifts from 512 nm to 511 nm after introducing the CDs, and the PL peak intensity slightly decreases at the wavelength around 540 nm (Figure 2a), which can be ascribed to defect passivation by plentiful amine groups from CDs.<sup>32</sup> Both samples, with and without CDs, show a high PL quantum yield (PL QY) of around 80% (Figure S9 in the Supporting Information shows a photograph of these bright green emitting films), indicating that traps of perovskite films on bare PEDOT:PSS belong to shallow ones, which can still participate in radiative recombination and cause only a slight decrease in

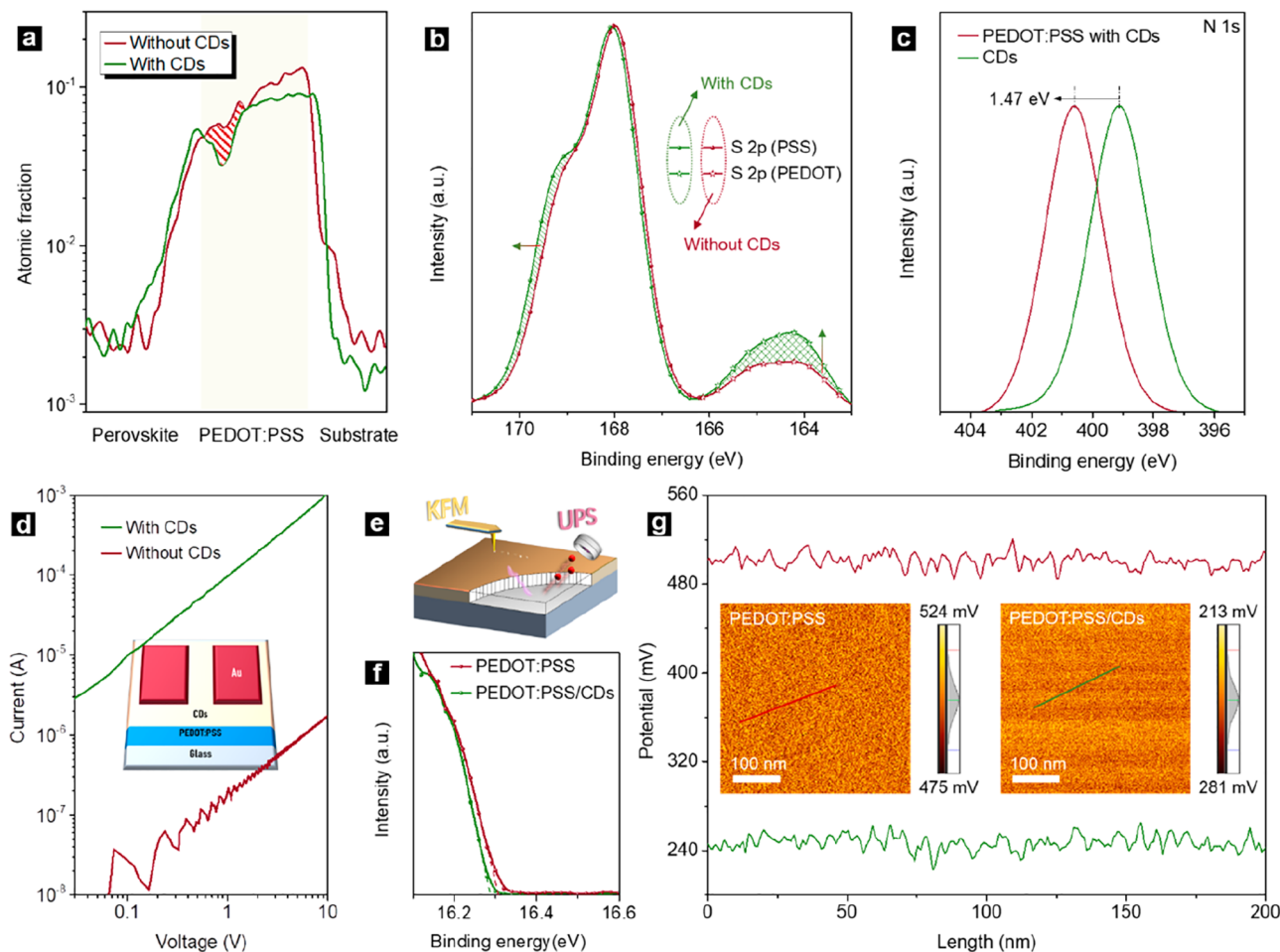


**Figure 3.** CDs change the surface properties of PEDOT:PSS *via* hydrogen bond interactions. (a) EDS curves for the S element of substrate/PEDOT:PSS/{with or without CDs}/Q-2D perovskite devices. (b) Normalized XPS spectra for S 2p of PEDOT:PSS with and without CDs. (c) Normalized XPS spectra for N 1s of CDs with and without PEDOT:PSS. (d) Current–voltage curves of the lateral structured devices testing the surface hole conductivity of PEDOT:PSS with and without CDs, with the respective structure as shown in the panel. The thickness of the PEDOT:PSS film is ~30 nm; the CD film consists of about a monolayer of CDs; the thickness of the Ag electrode is ~100 nm; the electrode separation distance is ~80  $\mu$ m. (e) Scheme illustrating the difference between KFM and UPS measurements, with KFM providing the film surface potential, while UPS reveals the work function position of the bulk semiconductor. (f) UPS spectra of PEDOT:PSS films with and without CDs on the surface. (g) KFM data for the same films as presented in (f): the insets are KFM maps showing the surface potential distribution, with colored lines (green, with CDs; red, without CDs) presenting surface potential changes illustrated by curves of the same color in the main graph.

photon energy of the PL. Taking this observation together with previous TEM and XRD results, we infer that CDs mainly affect the perovskite crystal quality and film composition. In perovskites, the better crystallization leads to a longer carrier lifetime.<sup>37</sup> The average recombination lifetime ( $\tau_{\text{avg}}$ ) of the Q-2D perovskite films were obtained from the PL decay curves shown in Figure 2b, fitted using a three-exponential function (see Table S1 in the Supporting Information). A value of  $\tau_{\text{avg}}$  equal to 7.59 ns for a CD-assisted film constitutes a 6.6-fold increase as compared to the bare PEDOT:PSS-based Q-2D perovskite film (1.15 ns), in line with the enhanced perovskite crystal quality after introducing the CDs.

TA spectra shown in Figure 2c reveal how the CDs influence the dynamics of photogenerated carriers within the Q-2D perovskite films. The TA spectra can be roughly divided into three regions based on the difference of bandgap energy between different  $n$  phases, namely, the  $n \leq 2$  region in the wavelength range of less than 475 nm, the  $n = 3$  region from 475 to 490 nm, and the  $n \geq 4$  region in the wavelength range

of greater than 490 nm. For a perovskite film grown on bare PEDOT:PSS, the exciton resonance at the  $n \leq 2$  region persists at 546 fs, representing exciton accumulation, which results from the incomplete energy transfer between the  $n \leq 2$  phases and  $n > 2$  phases. For a CD-assisted perovskite film, the exciton resonance at the  $n \leq 2$  region does not appear, representing an efficient energy transfer toward the large  $n$  phases or simply due to the reducing of  $n \leq 2$  phases. A ~10 nm redshift of the transient bleach minimum is observed from 157 fs to 10.4 ps for the film without CDs, while this value is ~1 nm for the CD-assisted perovskites, implying less reorganization during the bleach recovery. Besides, at 10.4 ps the exciton bleach mainly appears in the  $n \geq 4$  region for the CD-assisted perovskite film, while there is still a considerable peak intensity left in the  $n = 3$  region for the perovskite film on bare PEDOT:PSS, indicating that an accelerated exciton energy transfer occurs in the CD-assisted perovskite films. Thus, introduction of CDs enables formation of orderly arranged closely packed penetrating crystals and allows for

rapid and efficient exciton energy transfer to the smaller-bandgap phases.

The film composition also influences the energy transfer and carrier transport, since wide-bandgap impurities can block charge carriers, while narrow-bandgap impurities tend to trap those carriers. X-ray photoelectron spectroscopy (XPS) was used to reveal the chemical composition of films. As shown in Figure 2d, a peak belonging to CsBr in the XPS spectra of Br 3d<sup>38</sup> and peaks belonging to PbBr<sub>2</sub> in the XPS spectra of Pb 4f<sup>39</sup> are observed for the Q-2D perovskite film grown on bare PEDOT:PSS, while these impurities disappear after the introduction of the CDs as an intermediate layer. The appearance of CsBr and PbBr<sub>2</sub> in the perovskite film grown on bare PEDOT:PSS was further confirmed by HRTEM. Lattice spacings of 3.0 Å (Figure S10a in the Supporting Information) and 6.1 Å (Figure S10b in the Supporting Information) are observed, which correspond to the (110) crystal plane of CsBr and the (011) crystal plane of PbBr<sub>2</sub>, respectively. This phenomenon is attributed to the random orientation of grains formed during perovskite crystallization, which separate raw materials by the initially formed crystals, leading to incomplete precursor reaction and thereby the occurrence of CsBr and PbBr<sub>2</sub> impurities in the final perovskite. On the other hand, the CDs function as heterogeneous nucleation centers weakening the influence of uneven crystallization that prevails on solvent volatilization and allows more homogeneous growth of the Q-2D perovskites, which enables more complete reaction between the raw materials and avoids the formation of CsBr and PbBr<sub>2</sub>, which is evidenced by the disappearance of the XPS peak at ~68.2 eV belonging to Br 3d of CsBr<sup>38</sup> and peaks at ~138.8 and ~143.8 eV belonging to Pb 4f of PbBr<sub>2</sub><sup>39</sup> after introducing CDs (Figure 2d), in line with the promoted crystal quality. Meanwhile, strong signals of C 1s and O 1s peaks attributed to the PEO polymer have been detected in the bare PEDOT:PSS/Q-2D perovskite sample, while they disappeared in the CD-assisted perovskite film (Figure 2d). Also, the N 1s peak assigned to BA<sup>+</sup> appears in the CD-assisted perovskite film, which is stronger than that of the PEDOT:PSS/Q-2D perovskite film (Figure 2d), in line with the out-of-plane orientation of the Q-2D perovskite structure.

Thus, with the aid of CDs, high-quality vertically oriented crystals without grain boundaries are formed, impurities from side reactions are suppressed, and an insulating polymer capping at the perovskite film surface are removed, as illustrated schematically in Figure 2e, which enhances the energy transfer process and promotes the charge injection efficiency. This has been confirmed by current–voltage characterizations over a series of designed devices. Hole-only devices employing a structure of ITO/PEDOT:PSS/{with or without CDs}/perovskites/MoO<sub>x</sub>/Ag were fabricated. As shown in Figure 2f, in devices with CDs, the hole mobilities were enhanced by nearly 3.5 times from  $1.7 \times 10^{-6}$  cm<sup>2</sup> V<sup>-1</sup> s<sup>-1</sup> to  $5.9 \times 10^{-6}$  cm<sup>2</sup> V<sup>-1</sup> s<sup>-1</sup>, along with a decrease in hole trap densities from  $5.47 \times 10^{15}$  cm<sup>-3</sup> to  $3.78 \times 10^{15}$  cm<sup>-3</sup> (see characterizations for details). Electron-only devices with a structure of ITO/{with or without CDs}/perovskites/LiF/Al were fabricated. As shown in Figure S11 in the Supporting Information, in devices with CDs, the electron mobilities were improved by more than two times, from  $3.2 \times 10^{-6}$  cm<sup>2</sup> V<sup>-1</sup> s<sup>-1</sup> to  $7.8 \times 10^{-6}$  cm<sup>2</sup> V<sup>-1</sup> s<sup>-1</sup>. Lateral structure devices assessing the electron transport ability along the Q-2D perovskite film surface with the structure shown in the inset

of Figure 2g were also fabricated and studied. Under comparable test conditions, the currents of devices with CDs were nearly 10 times higher than that of bare PEDOT:PSS-based ones, as a result of the lack of any formation of the insulating PEO polymer on the Q-2D perovskite film surface with that layer structure. These data confirmed improvements in charge transport in Q-2D perovskites formed on top of an interlayer of CDs.

The charge transfer process from the HTL to the emitting layer is an important issue influencing LED performance. The PEDOT:PSS HTL is composed of conductive PEDOT molecules and an insulating PSS polymer, where PEDOT is typically capped by PSS via Coulomb interactions to avoid aggregation.<sup>40</sup> During the FIB-TEM characterization of the Q-2D perovskites as shown in Figure S6, we also conducted energy-dispersive X-ray spectroscopy (EDS) to confirm the element distributions. As shown in the insets of Figure S6c and f in the Supporting Information, we can clearly distinguish each layer by their characteristic elements. Significantly, the distribution of S, which is the characteristic chemical element of both the PEDOT and PSS, presents different distribution profiles at the HTL/perovskites interface as a result of the presence or absence of CDs. The relevant EDS curves of the S element are extracted and presented in Figure 3a. Clearly, the inclusion of the CDs leads to a decrease of S content at the HTL/perovskite interface.

To better understand the effect of the CDs on PEDOT:PSS, XPS spectra were taken on PEDOT:PSS films with and without CDs. While both the PEDOT and PSS contain the S element, the distinguishing feature is that sulfur from PSS appears at a higher binding energy compared with the case for PEDOT, which is caused by the attraction of the oxygen atoms to the sulfur in the sulfonic functional group. Figure 3b shows normalized XPS spectra for S 2p: the peak at ~168 eV shifts to higher energy, and the peak at ~165 eV becomes stronger after introducing the CDs. These changes correspond to PSS forming stronger hydrogen bonds with the CDs than the Coulomb forces it experiences with PEDOT, so that more PEDOT units are exposed rather than capped by PSS, respectively. More detailed XPS analysis of the S 2p peaks is given in Figure S12a (Supporting Information). How the CDs interact with PEDOT:PSS is ascertained by analyzing the N 1s peaks for CD layers with and without PEDOT:PSS. As shown in Figure 3c, the N 1s peak of the CDs shifts toward a higher energy of 1.47 eV with the inclusion of PEDOT:PSS, which is caused by the protonation of the amine group to form  $-\text{NH}_3^+$ , indicating that the rich population of  $-\text{NH}_2$  groups on the CD surface plays an important role here.<sup>41</sup> Detailed XPS analysis of the N 1s peaks is shown in Figure S12b (Supporting Information). The distribution of PEO simply follows the pattern of perovskites, since PEO tends to cover the perovskite crystals along the direction parallel to the planes, as a result of minimizing the surface energy. Thus, the surface content of PEO decreases after the introduction of CDs, where the perovskite crystals penetrate the vertical direction of the device and PEO distributes preferentially at the grain boundaries. The bonding of the CDs with sulfonic groups in PSS weakens the Coulomb interaction between PSS and PEDOT, which is beneficial to the conductivity of the HTL (Figure 3d) and has been confirmed by testing the current–voltage behavior of lateral devices using the structure given as the inset of Figure 3d. As a result, over 500 times improvement in hole transport

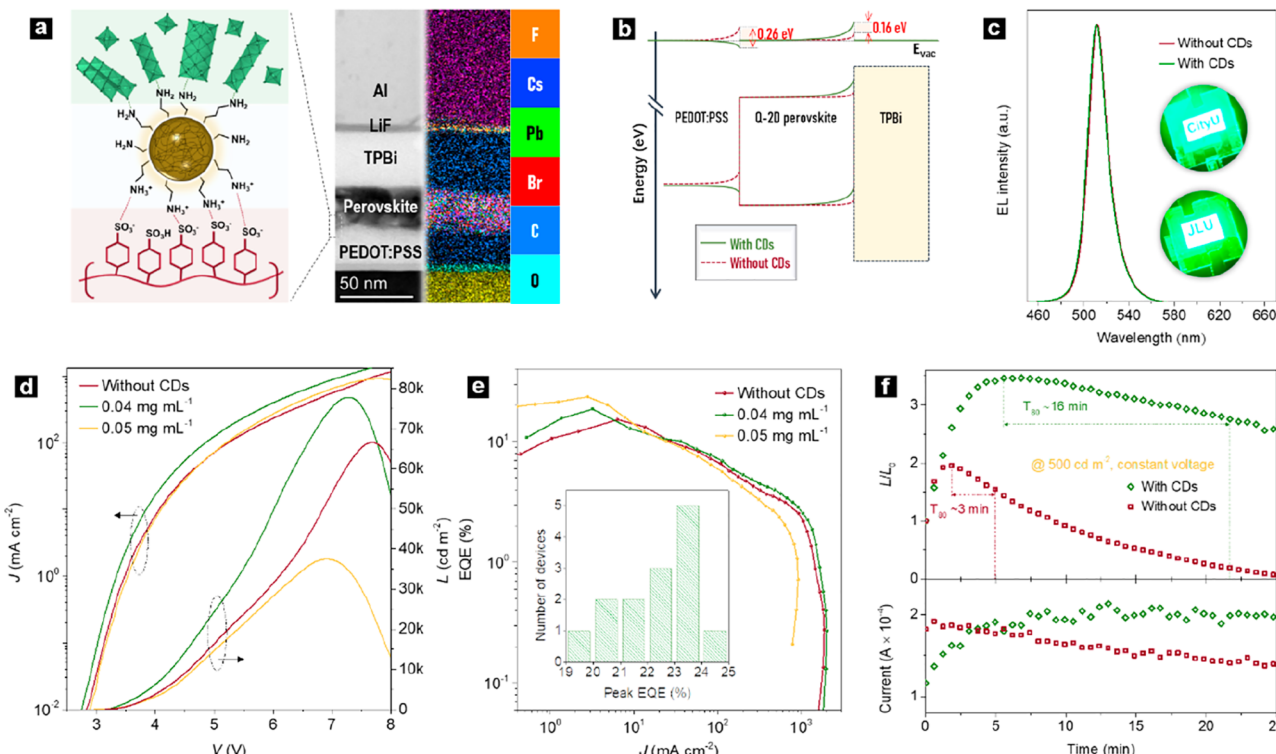


**Figure 4.** Q-2D perovskite LED performance and operational stability. (a) Schematic diagram showing how CDs link the Q-2D perovskites with PEDOT:PSS via hydrogen bonds (left) and cross-sectional TEM image of the Q-2D perovskite LEDs alongside with the corresponding element mapping (right). (b) Band energy diagram for PEDOT:PSS HTL, Q-2D perovskite emitting layer, and TPBi electron transport layer, comparing the differences in charge injection between devices with or without CDs. (c) EL spectra of the LEDs with and without CDs, with photographs showing two working devices (both with CDs) at an applied voltage of 5 V. (d) Current density ( $J$ ) and brightness ( $L$ ) vs driving voltage ( $V$ ) and (e) EQE vs  $J$  of LEDs without CDs and with CD interlayers prepared using two different concentrations of CDs, namely,  $0.04$  and  $0.05\text{ mg mL}^{-1}$  solutions. The inset in (e) shows peak EQEs collected from 14 devices. (f) Data of operational stability tests of the LEDs with and without CDs at the same initial luminance under a constant voltage. The term  $L_0$  stands for the initial brightness, here  $500\text{ cd m}^{-2}$ . Synchronous luminance and current change versus operation time of LEDs are given in the top and bottom frame, respectively.

is achieved by simply spin-coating an ultrathin CD film over the PEDOT:PSS layer.

For the purpose of identifying the influence of CDs on the semiconducting properties of PEDOT:PSS, we combined ultraviolet photoelectron spectroscopy (UPS) measurements to determine the work function position of the bulk films with Kelvin probe force microscopy (KFM) to determine the film surface potential (Figure 3e). After introducing CDs, the work function only slightly downshifts from  $-4.90\text{ eV}$  to  $-4.92\text{ eV}$  (Figure 3f), while the surface potential significantly downshifts from  $-4.70\text{ eV}$  to  $-4.96\text{ eV}$  (Figure 3g). This indicates that the introduction of CDs greatly changes the surface property of PEDOT:PSS films while maintaining their bulk semiconducting properties. The large difference in surface potential between PEDOT:PSS and PEDOT:PSS/CDs films is attributed to the changes in the surface chemical composition: the more PSS on the surface, the higher the surface potential, while the more PEDOT that is exposed, the lower the surface potential.<sup>41</sup> As a result, with the aid of CDs, the PEDOT:PSS film acquires a higher surface conductivity and a lower surface potential, which are beneficial for hole transport and injection in perovskite LEDs.

The above comprehensive characterization of Q-2D perovskite LEDs allows us to draw a full picture of how CDs assist the construction of the hydrogen bond interfaces. As illustrated in Figure 4a, CDs on one hand release PEDOT from PSS capping and are anchored by PSS via hydrogen bonds on the

surface of the HTL. On the other hand, the CDs interact with intermediates from the perovskite raw materials, enabling the out-of-plane oriented growth of penetrating Q-2D perovskites as well as suppressing the appearance of impurities from incomplete perovskite precursor conversion (see Figure 2e), which promotes the energy transfer, charge carrier injection, and transport processes within the LEDs (see Figure S5 in the Supporting Information). The elemental mapping conducted over the Q-2D perovskite LED (shown on the right side of Figure 4a) provides the distribution of F, Cs, Pb, Br, C, and O elements, resolving the details of their planar-type multilayer structure. The respective energy band diagram for all constituting layers is given in Figure 4b. Based on the UPS and KFM results (Figure 3f and g), the presence of CDs results in a reduction of the hole-injection barrier from PEDOT:PSS to perovskites of  $0.26\text{ eV}$ , which improves the hole injection efficiency. We also combined UPS with KFM in analyzing the semiconducting properties of Q-2D perovskites. As shown in Figure S13a (Supporting Information), the UPS results show that CDs do not change the work function ( $-5.01\text{ eV}$ ) positions of the Q-2D perovskites, while in Figure S13b (Supporting Information), the KFM results show that CDs upshift the surface potential of the Q-2D perovskites from  $-5.44\text{ eV}$  to  $-5.28\text{ eV}$ . So, with the aid of CDs, the electron injection gap from TPBi to perovskites has been reduced by  $0.16\text{ eV}$ , mainly due to the nonappearance of the surface capping insulating PEO polymer in that instance (Figure 2e).

Since surface roughness of functional layers is important for LED performance, we characterized PEDOT:PSS and perovskite films, both with and without the addition of CDs, by atomic force microscopy (AFM). As shown in Figure S14 in the Supporting Information, introduction of CDs has very little effect on the surface morphology. The root-mean-square (RMS) value of the PEDOT:PSS film only slightly increases from 1.29 nm to 1.94 nm after CDs are introduced. The RMS value of perovskite films only slightly increases from 1.53 nm to 1.67 nm after CDs are introduced. In the Q-2D perovskite LEDs, the optimized thicknesses are around 30, 30, 40, 1, and 100 nm for the PEDOT:PSS, Q-2D perovskite, TPBi, LiF, and Al layers, respectively. LEDs without a CD interlayer show bright green EL centered at 512 nm originating solely from the Q-2D perovskite emitters (Figure 4c). The introduction of CDs slightly blue-shifts the EL peak for less than 1 nm, and the symmetric emission peak at  $\sim$ 511 nm with a narrow full-width at half-maximum of 20 nm corresponds to Commission International de l'Eclairage (CIE) color coordinates of (0.18, 0.57). EL spectra (Figure S15 in the Supporting Information) show no obvious shifts upon changing the operating voltage of LEDs. The insets in Figure 4c present photographs of green-emitting devices with the City University of Hong Kong (CityU) and Jilin University (JLU) logos operated under  $\sim$ 5 V bias. Figure 4d shows the current density–voltage–luminance ( $J$ – $V$ – $L$ ) characteristics of LEDs employing CD films prepared using two different concentrations of CDs, namely, 0.04 and 0.05 mg mL<sup>-1</sup> solutions. Just as we inferred, the systematic effects of the CDs considerably promote the EL performances of these LEDs. With a CD film prepared using a 0.04 mg mL<sup>-1</sup> solution, the device brightness increases from 70 687 cd m<sup>-2</sup> to 80 086 cd m<sup>-2</sup>, while with a CD film prepared using a 0.05 mg mL<sup>-1</sup> solution, the peak EQE increases from 15.3% to 24.5% (Figure 4e) as compared to devices without CDs. The current density increases faster for the device with CDs (0.04 mg mL<sup>-1</sup>), showing that the respective LEDs possess higher charge injection efficiency. Note that although slightly increasing the CD concentration from 0.04 mg mL<sup>-1</sup> to 0.05 mg mL<sup>-1</sup> leads to a higher EQE, it also brings a faster efficiency decline. This is because a more concentrated CD solution leads to a higher density of anchored CDs serving as nucleation centers for the perovskites, which decreases the crystal size and thus increases the binding energy. Although this is beneficial for radiative recombination under low carrier concentrations, it would also greatly facilitate crystal charging under high carrier concentrations. Importantly, the CD-assisted devices have shown high reproducibility. As shown in the inset of Figure 4e, over half of the LEDs in the set of 14 offer high EQEs of around 23%.

We estimated the LED operational stability at an initial luminance of 500 cd m<sup>-2</sup> under a constant voltage, following the advice on measuring the lifetime of perovskite LEDs given by Lee and co-workers.<sup>42</sup> The  $T_{80}$  value, defined as the time for the luminance to decrease to 80%  $L_{\max}$  (the maximum value of luminance during operation), is extended by over 5 times (from 3 min to 16 min) after the introduction of CDs (Figure 4f), which is attributed to the reduction of joule heating during operation caused by the decrease of grain boundary defects. Since devices with CDs have a higher efficiency than devices without CDs, they require a lower driving current to reach the same initial luminance. At the initial stage of operation, both devices experience an increase in brightness and current, as a result of electric field driven ion redistribution. The increase

lasts longer for the LED with CDs, which may be caused by the suppression of ion migration due to the anchoring effect of Br<sup>-</sup> ions by CDs via hydrogen bonds. Ion migration in polycrystalline perovskites preferentially occurs through the grain boundaries and results in the change of the ion ratio on the crystal surface, generating the surface traps. Once the ion distribution equilibrium is reached again, the charge transport is more severely affected by defective crystal surfaces in randomly arranged perovskites, while it is less affected in the vertically oriented Q-2D perovskites because carrier tunneling/hopping between the adjacent crystals is avoided. The initial increase in brightness is followed by its decline, which is significantly slower for the LED employing CDs than for the devices without CDs, with the former also showing higher current. The suppression of carriers' losses through a nonradiative recombination process in LEDs with CDs is also seen from evaluation of the temperature of devices under operation. As shown in Figure S16 (Supporting Information), the temperature of LEDs with CDs is  $\sim$ 3 °C lower than that of the devices without CDs after operation under a constant voltage of 4 V for 5 min. Thermal-induced emission quenching is one of the key issues preventing realization of perovskite LEDs with simultaneously high brightness and efficiency; thus, our approach of using CDs, combined with recently reported demonstrations,<sup>43–46</sup> offers opportunities for extending the lifetime of perovskite LEDs.

## CONCLUSIONS

Our work showcases the construction of a hydrogen-bond-assisted interface for Q-2D perovskite LEDs with an aid of ultrasmall amine-terminated CDs, which allows stronger interaction between the HTL and emitting layers, enabling vertically oriented growth of Q-2D perovskites and promotion in crystal quality, as well as an elimination of unfavorable factors to carrier transport and injection, thus leading to highly efficient EL emission along with significantly enhanced device operational stability. Our results suggest that the solution-processed devices can embrace a large performance improvement by replacing the common van der Waals interfaces of the typical functional layers with more strongly coupled interfaces.

## METHODS

**Materials.** All chemicals were used as received without further purification. PEDOT:PSS (4083) and TPBi were purchased from Xi'an Polymer. CsBr (99.999%) was obtained from Alfa Aesar, and PbBr<sub>2</sub> from Tokyo Chemical Industry. PEO, DMSO, BABr ( $\geq$ 98%), LiF, and 2-methoxyethanol were purchased from Sigma-Aldrich. Citric acid (CA, 99.5%) and ethylenediamine (EDA, 99.0%) were obtained from Aladdin.

**Synthesis of CDs.** The synthetic method to produce the CDs followed the previous report.<sup>47</sup> A 576 mg amount of CA and 600  $\mu$ L of EDA were dissolved in deionized water, and the mixture was heated in a poly(tetrafluoroethylene)-lined autoclave at 200 °C for 8 h. After cooling, the obtained solution was concentrated and dialyzed against deionized water within a dialysis bag (3500 molecular weight cutoff) for 2 days. During this period, the deionized water was changed every 5–6 h. Finally, CD powders were obtained through lyophilization.

**Q-2D Perovskite Precursor Solutions.** CsBr, PbBr<sub>2</sub>, and BABr were dissolved into DMSO in the ratio as previously reported.<sup>33</sup> Then, PEO was added to the solution until a specific gravity of 1 mg mL<sup>-1</sup> was reached. The mixture was heated and homogenized at 60 °C for 4 h. All procedures were carried out in an argon-filled glovebox.

**Device Fabrication.** ITO glass substrates were sonicated in sequence with detergent, deionized water, ethanol, acetone, and isopropyl alcohol for 10 min. These substrates were dried under

nitrogen flow and then treated with an oxygen-plasma for 15 min. A PEDOT:PSS layer was spin-coated onto ITO substrates at 4000 rpm for 40 s, followed by annealing at 150 °C for 15 min in air. A CD solution was spin-coated on top of the PEDOT:PSS layer at 4000 rpm for 40 s, followed by annealing at 130 °C to vaporize the solvent. After that, the substrates were quickly transferred into an argon-filled glovebox to prepare the Q-2D perovskite films, by spin-coating 50 μL of precursor solution at 4000 rpm for 40 s, followed by baking at 80 °C for 5 min. After that, TPBi, LiF, and Al electrode layers were sequentially deposited on top of the Q-2D perovskite film by thermal evaporation under a vacuum of  $\sim 1 \times 10^{-4}$  Pa. The lateral structured devices were fabricated on glass substrates, with the electrode separation distance around 80 μm.

**Characterization.** FTIR spectra were collected on an IFS-66 V/S spectrophotometer. XRD patterns were collected on a Bruker SMART-CCD diffractometer. The perovskite films for XRD measurement were grown on Si substrates. The FIB samples were prepared by a Helios 5 ux. A Ga ion beam was used to process the pretreated sample at 30 kV and 9.1 nA, and the dimensions of the initial films were 10 μm by 8 μm by 2 μm. Meticulous pruning of the sample was carried out in several steps: first, a 30 kV, 0.26 nA ion beam was used to thin the sample to 170 nm; then, a 8 kV, 61 pA ion beam was used to thin the sample to 80 nm; finally, a 5 kV, 61 pA ion beam was used to obtain the sample to be tested at about 50 nm thickness. A double Cs-corrected TEM (JEM ARM300F GRAND ARM) operated at a voltage of 300 kV was employed in the CD characterizations. The TEM images and EDS mappings were obtained on a Talos F 200× microscope. The samples were prepared by multilayer deposition on top of Si substrates. Absorption spectra were measured on a UV-2600 spectrophotometer (Shimadzu). PL spectra were obtained on a QE Pro spectrometer from Ocean Optics (with an excitation wavelength of 365 nm). GIWAXS were measured at beamline BL14B1 of the Shanghai Synchrotron Radiation Facility, China. PL QYs were measured using an integrating sphere equipped with a QE Pro spectrometer in a nitrogen-filled glovebox, and the samples were excited using a 405 nm laser with an intensity of 1.3 mW. AFM images were collected on a SII Nanonavi probe station (300 hv). Time-resolved PL measurements were performed on the time-correlated single-photon-counting system of the FLS920P Edinburgh spectrometer with the excitation wavelength of 400 nm. TA spectra were measured on a Helios Fire femtosecond transient absorption pump–probe spectrometer (Ultrafast Systems LLC) with 420 nm pump wavelength and 100 fs pump temporal pulse, respectively. The perovskite films for TA characterization were fabricated on quartz substrates. XPS and UPS were performed using the PREVAC system. The samples for XPS and UPS were prepared on ITO substrates. KFM images were collected on an AFM5100N instrument. The samples were prepared on top of Si substrates. The EL characteristics of the Q-2D perovskite LEDs were collected on a system comprising a Keithley 2612 m coupled with a PR-670 Spectra Scan spectroradiometer and a Newport 918-D-SLOD3R silicon photodiode.

EQE is defined as the ratio of the number of input electrons to the number of output photons of the device,<sup>48</sup> namely,

$$\text{EQE} = \frac{N_p}{N_e}$$

$N_e$  can be calculated from the expression  $N_e = \frac{I}{e}$ , where  $e$  stands for the electron charge and  $I$  is the current density.  $N_p$  can be determined using the equation  $N_p = \frac{\pi L \int I(\lambda) d\lambda}{Khc \int I(\lambda) K(\lambda) d\lambda}$ , where  $h$  is the Planck constant,  $c$  is the speed of light in a vacuum,  $\lambda$  is the wavelength of emitting photons,  $I(\lambda)$  is the function of the EL spectrum,  $K(\lambda)$  is the function of the emission wavelength, which shows the relative sensitivity of the human eye to different colors,  $K$  is the conversion factor given as 683 lm/W, and  $L$  is the device brightness.

Infrared and visible photographs during the device operational stability characterization were obtained using an FLIR-E6390 thermal imaging system. All the device characterization tests were carried out

on nonencapsulated devices at room temperature in a N<sub>2</sub>-filled glovebox. The current–voltage characterization of the hole-only devices was done with a Keithley 2612 source meter. The trap-state densities were calculated using the following equation:  $V_{TFL} = \frac{eN_t L^2}{2\epsilon\epsilon_0}$

The charge mobilities ( $\mu$ ) were obtained by fitting the dark current using the Mott–Gurney law:  $J = \frac{9}{8}\epsilon\epsilon_0\mu\frac{V^2}{L^3}$  where  $V_{TFL}$  represents the voltage at which all the traps are filled;  $\epsilon$  and  $\epsilon_0$  represent perovskite permittivity and vacuum permittivity, respectively;  $L$  is the thickness of the film;  $N_t$  represents defect density;  $J$  and  $V$  represent dark current and voltage, respectively.

## ASSOCIATED CONTENT

### SI Supporting Information

The Supporting Information is available free of charge at <https://pubs.acs.org/doi/10.1021/acsnano.2c03064>.

Schematic diagram of the formation of perovskite films on top of HTL or HTL/CDs layers; TEM image, FTIR spectrum, and UV-vis absorption spectrum of CDs; PL spectrum of Q-2D perovskite; schematic illustration of the growth of a perovskite layer; illustration of the process of carrier transport; TEM images of the Q-2D perovskite LEDs; GIWAXS patterns; XRD patterns; photograph of perovskite films; HRTEM images of the Q-2D perovskite layer of an LED made without CDs; current–voltage curves of the “electron-only” devices; XPS spectra of PEDOT:PSS and CDs; UPS spectra and KFM characterizations of perovskite films; AFM of the HTL and the perovskite films; EL spectra of LEDs operated under different bias; surface temperature monitoring of Q-2D perovskite LEDs; fitting details of PL decay curves (PDF)

## AUTHOR INFORMATION

### Corresponding Authors

Xiaoyu Zhang – Key Laboratory of Automobile Materials, Ministry of Education, College of Materials Science and Engineering, Jilin Provincial International Cooperation Key Laboratory of High-Efficiency Clean Energy Materials, Electron Microscopy Center, Jilin University, Changchun 130012, People's Republic of China;  [orcid.org/0000-0001-7528-4405](https://orcid.org/0000-0001-7528-4405); Email: [zhangxiaoyu@jlu.edu.cn](mailto:zhangxiaoyu@jlu.edu.cn)

Andrey L. Rogach – Department of Materials Science and Engineering and Centre for Functional Photonics (CFP), City University of Hong Kong, Hong Kong SAR 999077, People's Republic of China; Shenzhen Research Institute, City University of Hong Kong, Shenzhen 518057, People's Republic of China;  [orcid.org/0000-0002-8263-8141](https://orcid.org/0000-0002-8263-8141); Email: [andrey.rogach@cityu.edu.hk](mailto:andrey.rogach@cityu.edu.hk)

Weitao Zheng – Key Laboratory of Automobile Materials, Ministry of Education, College of Materials Science and Engineering, Jilin Provincial International Cooperation Key Laboratory of High-Efficiency Clean Energy Materials, Electron Microscopy Center, Jilin University, Changchun 130012, People's Republic of China; Email: [wtzheng@jlu.edu.cn](mailto:wtzheng@jlu.edu.cn)

### Authors

Wei Dong – Key Laboratory of Automobile Materials, Ministry of Education, College of Materials Science and Engineering, Jilin Provincial International Cooperation Key Laboratory of High-Efficiency Clean Energy Materials,

Electron Microscopy Center, Jilin University, Changchun 130012, People's Republic of China

Fan Yang – State Key Laboratory of Supramolecular Structure and Materials, College of Chemistry, Jilin University, Changchun 130012, People's Republic of China

Qingsen Zeng – State Key Laboratory of Supramolecular Structure and Materials, College of Chemistry, Jilin University, Changchun 130012, People's Republic of China; [ORCID: 0000-0002-0877-0814](https://orcid.org/0000-0002-0877-0814)

Wenxu Yin – Key Laboratory of Automobile Materials, Ministry of Education, College of Materials Science and Engineering, Jilin Provincial International Cooperation Key Laboratory of High-Efficiency Clean Energy Materials, Electron Microscopy Center, Jilin University, Changchun 130012, People's Republic of China

Wei Zhang – Key Laboratory of Automobile Materials, Ministry of Education, College of Materials Science and Engineering, Jilin Provincial International Cooperation Key Laboratory of High-Efficiency Clean Energy Materials, Electron Microscopy Center, Jilin University, Changchun 130012, People's Republic of China; [ORCID: 0000-0002-6414-7015](https://orcid.org/0000-0002-6414-7015)

Haoran Wang – Key Laboratory of Advanced Display and System Applications of Ministry of Education, Shanghai University, Shanghai 200072, People's Republic of China

Xuyong Yang – Key Laboratory of Advanced Display and System Applications of Ministry of Education, Shanghai University, Shanghai 200072, People's Republic of China; [ORCID: 0000-0003-3597-1491](https://orcid.org/0000-0003-3597-1491)

Stephen V. Kershaw – Department of Materials Science and Engineering and Centre for Functional Photonics (CFP), City University of Hong Kong, Hong Kong SAR 999077, People's Republic of China; [ORCID: 0000-0003-0408-4902](https://orcid.org/0000-0003-0408-4902)

Bai Yang – State Key Laboratory of Supramolecular Structure and Materials, College of Chemistry, Jilin University, Changchun 130012, People's Republic of China; [ORCID: 0000-0002-3873-075X](https://orcid.org/0000-0002-3873-075X)

Complete contact information is available at:  
<https://pubs.acs.org/10.1021/acsnano.2c03064>

## Author Contributions

X.Y.Z., A.L.R., and W.T.Z. designed and directed the study. W.D. and F.Y. fabricated and characterized LEDs. Q.S.Z. synthesized the CDs. S.V.K. analyzed the TA data. W.D., X.Y.Z., F.Y., Q.S.Z., W.X.Y., W.Z., H.R.W., X.Y.Y., S.V.K., B.Y., A.L.R., and W.T.Z. analyzed and discussed the experimental results. All authors contributed to writing the manuscript.

## Notes

The authors declare no competing financial interest.

## ACKNOWLEDGMENTS

The authors acknowledge financial support from the National Natural Science Foundation of China (51972136, 52072141, 22035001), Interdisciplinary Integration and Innovation Project of JLJU (JLUXKJC2021QZ12), the Research Grant Council of Hong Kong (C7035-20G), the Croucher Foundation of Hong Kong, and the Science Technology and Innovation Committee of Shenzhen Municipality (JCYJ20190808181201899).

## REFERENCES

- (1) Tan, Z.; Moghaddam, R. S.; Lai, M. L.; Docampo, P.; Higler, R.; Deschler, F.; Price, M.; Sadhanala, A.; Pazos, L. M.; Credgington, D.; Hanusch, F.; Bein, T.; Snaith, H. J.; Friend, R. H. Bright Light-Emitting Diodes Based on Organometal Halide Perovskite. *Nat. Nanotechnol.* **2014**, *9*, 687–692.
- (2) Cho, H.; Jeong, S.-H.; Park, M.-H.; Kim, Y.-H.; Wolf, C.; Lee, C.-L.; Heo, J. H.; Sadhanala, A.; Myoung, N.; Yoo, S.; Im, S. H.; Friend, R. H.; Lee, T.-W. Overcoming the Electroluminescence Efficiency Limitations of Perovskite Light-Emitting Diodes. *Science* **2015**, *350*, 1222.
- (3) Ma, D.; Lin, K.; Dong, Y.; Choubisa, H.; Proppe, A. H.; Wu, D.; Wang, Y.-K.; Chen, B.; Li, P.; Fan, J. Z.; Yuan, F.; Johnston, A.; Liu, Y.; Kang, Y.; Lu, Z.-H.; Wei, Z.; Sargent, E. H. Distribution Control Enables Efficient Reduced-Dimensional Perovskite LEDs. *Nature* **2021**, *599*, 594–598.
- (4) Xu, W.; Hu, Q.; Bai, S.; Bao, C.; Miao, Y.; Yuan, Z.; Borzda, T.; Barker, A. J.; Tyukalova, E.; Hu, Z.; Kawecki, M.; Wang, H.; Yan, Z.; Liu, X.; Shi, X.; Uvdal, K.; Fahlman, M.; Zhang, W.; Duchamp, M.; Liu, J.-M.; Petrozza, A.; Wang, J.; Liu, L.-M.; Huang, W.; Gao, F. Rational Molecular Passivation for High-Performance Perovskite Light-Emitting Diodes. *Nat. Photonics* **2019**, *13*, 418–424.
- (5) Yoo, J.; Seo, G.; Chua, M. R.; Park, T. G.; Lu, Y.; Rotermund, F.; Kim, Y.-K.; Moon, C. S.; Jeon, N. J.; Correa-Baena, J.-P.; Bulović, V.; Shin, S. S.; Bawendi, M. G.; Seo, J. Efficient Perovskite Solar Cells via Improved Carrier Management. *Nature* **2021**, *590*, 587–593.
- (6) Kim, Y.; Zhai, Y.; Lu, H.; Pan, X.; Xiao, C.; Gaulding, E. A.; Harvey, S. P.; Berry, J. J.; Vardeny, Z. V.; Luther, J. M.; Beard, M. C. Chiral-Induced Spin Selectivity Enables a Room-Temperature Spin Light-Emitting Diode. *Science* **2021**, *371*, 1129–1133.
- (7) Kim, Y.; Kim, S.; Kakekhani, A.; Park, J.; Park, J.; Lee, Y.; Xu, H.; Nagane, S.; Wexler, R. B.; Kim, D.-H.; Jo, S. H.; Martínez-Sarti, L.; Tan, P.; Sadhanala, A.; Park, G.-S.; Kim, Y.-W.; Hu, B.; Bolink, H. J.; Yoo, S.; Friend, R. H.; Rappe, A. M.; Lee, T.-W. Comprehensive Defect Suppression in Perovskite Nanocrystals for High-Efficiency Light-Emitting Diodes. *Nat. Photonics* **2021**, *15*, 148–155.
- (8) Tsai, H.; Shrestha, S.; Vilá, R. A.; Huang, W.; Liu, C.; Hou, C.-H.; Huang, H.-H.; Wen, X.; Li, M.; Wiedermann, G.; Cui, Y.; Cotlet, M.; Zhang, X.; Ma, X.; Nie, W. Bright and Stable Light-Emitting Diodes Made with Perovskite Nanocrystals Stabilized in Metal-Organic Frameworks. *Nat. Photonics* **2021**, *15*, 843–849.
- (9) Hassan, Y.; Park, J. H.; Crawford, M. L.; Sadhanala, A.; Lee, J.; Sadighian, J. C.; Mosconi, E.; Shivanna, R.; Radicchi, E.; Jeong, M.; Yang, C.; Choi, H.; Park, S. H.; Song, M. H.; De Angelis, F.; Wong, C. Y.; Friend, R. H.; Lee, B. R.; Snaith, H. J. Ligand-Engineered Bandgap Stability in Mixed-Halide Perovskite LEDs. *Nature* **2021**, *591*, 72–77.
- (10) Zhao, B.; Bai, S.; Kim, V.; Lamboll, R.; Shivanna, R.; Auras, F.; Richter, J. M.; Yang, L.; Dai, L.; Alsari, M.; She, X.-J.; Liang, L.; Zhang, J.; Lilliu, S.; Gao, P.; Snaith, H. J.; Wang, J.; Greenham, N. C.; Friend, R. H.; Di, D. High-Efficiency Perovskite-Polymer Bulk Heterostructure Light-Emitting Diodes. *Nat. Photonics* **2018**, *12*, 783–789.
- (11) Chen, J.; Wang, J.; Xu, X.; Li, J.; Song, J.; Lan, S.; Liu, S.; Cai, B.; Han, B.; Precht, J. T.; Ginger, D.; Zeng, H. Efficient and Bright White Light-Emitting Diodes Based on Single-Layer Heterophase Halide Perovskites. *Nat. Photonics* **2021**, *15*, 238–244.
- (12) Liu, M.; Wan, Q.; Wang, H.; Carulli, F.; Sun, X.; Zheng, W.; Kong, L.; Zhang, Q.; Zhang, C.; Zhang, Q.; Brovelli, S.; Li, L. Suppression of Temperature Quenching in Perovskite Nanocrystals for Efficient and Thermally Stable Light-Emitting Diodes. *Nat. Photonics* **2021**, *15*, 379–385.
- (13) Du, P.; Li, J.; Wang, L.; Sun, L.; Wang, X.; Xu, X.; Yang, L.; Pang, J.; Liang, W.; Luo, J.; Ma, Y.; Tang, J. Efficient and Large-Area All Vacuum-Deposited Perovskite Light-Emitting Diodes via Spatial Confinement. *Nat. Commun.* **2021**, *12*, 4751.
- (14) Chiba, T.; Hayashi, Y.; Ebe, H.; Hoshi, K.; Sato, J.; Sato, S.; Pu, Y.-J.; Ohisa, S.; Kido, J. Anion-Exchange Red Perovskite Quantum Dots with Ammonium Iodine Salts for Highly Efficient Light-Emitting Devices. *Nat. Photonics* **2018**, *12*, 681–687.

- (15) Cherniukh, I.; Rainò, G.; Stöferle, T.; Burian, M.; Travasset, A.; Naumenko, D.; Amenitsch, H.; Erni, R.; Mahrt, R. F.; Bodnarchuk, M. I.; Kovalenko, M. V. Perovskite-Type Superlattices from Lead Halide Perovskite Nanocubes. *Nature* **2021**, *593*, 535–542.
- (16) Yuan, M.; Quan, L. N.; Comin, R.; Walters, G.; Sabatini, R.; Voznyy, O.; Hoogland, S.; Zhao, Y.; Beauregard, E. M.; Kanjanaboos, P.; Lu, Z.; Kim, D. H.; Sargent, E. H. Perovskite Energy Funnels for Efficient Light-Emitting Diodes. *Nat. Nanotechnol.* **2016**, *11*, 872–877.
- (17) Wang, N.; Cheng, L.; Ge, R.; Zhang, S.; Miao, Y.; Zou, W.; Yi, C.; Sun, Y.; Cao, Y.; Yang, R.; Wei, Y.; Guo, Q.; Ke, Y.; Yu, M.; Jin, Y.; Liu, Y.; Ding, Q.; Di, D.; Yang, L.; Xing, G.; Tian, H.; Jin, C.; Gao, F.; Friend, R. H.; Wang, J.; Huang, W. Perovskite Light-Emitting Diodes Based on Solution-Processed Self-Organized Multiple Quantum Wells. *Nat. Photonics* **2016**, *10*, 699–704.
- (18) Zou, Y.; Teng, P.; Xu, W.; Zheng, G.; Lin, W.; Yin, J.; Kobera, L.; Abbrent, S.; Li, X.; Steele, J. A.; Solano, E.; Roeffaers, M. B. J.; Li, J.; Cai, L.; Kuang, C.; Scheblykin, I. G.; Brus, J.; Zheng, K.; Yang, Y.; Mohammed, O. F.; Bakr, O. M.; Pullerits, T.; Bai, S.; Sun, B.; Gao, F. Manipulating Crystallization Dynamics through Chelating Molecules for Bright Perovskite Emitters. *Nat. Commun.* **2021**, *12*, 4831.
- (19) Cui, J.; Liu, Y.; Deng, Y.; Lin, C.; Fang, Z.; Xiang, C.; Bai, P.; Du, K.; Zuo, X.; Wen, K.; Gong, S.; He, H.; Ye, Z.; Gao, Y.; Tian, H.; Zhao, B.; Wang, J.; Jin, Y. Efficient Light-Emitting Diodes Based on Oriented Perovskite Nanoplatelets. *Sci. Adv.* **2021**, *7*, No. eabg8458.
- (20) Jagielski, J.; Kumar, S.; Wang, M.; Scullion, D.; Lawrence, R.; Li, Y.-T.; Yakunin, S.; Tian, T.; Kovalenko, M. V.; Chiu, Y.-C.; Santos, E. J. G.; Lin, S.; Shih, C.-J. Aggregation-Induced Emission in Lamellar Solids of Colloidal Perovskite Quantum Wells. *Sci. Adv.* **2017**, *3*, No. eaao2028.
- (21) Sun, C.; Jiang, Y.; Cui, M.; Qiao, L.; Wei, J.; Huang, Y.; Zhang, L.; He, T.; Li, S.; Hsu, H.-Y.; Qin, C.; Long, R.; Yuan, M. High-Performance Large-Area Quasi-2D Perovskite Light-Emitting Diodes. *Nat. Commun.* **2021**, *12*, 2207–2207.
- (22) Chu, Z.; Zhao, Y.; Ma, F.; Zhang, C.-X.; Deng, H.; Gao, F.; Ye, Q.; Meng, J.; Yin, Z.; Zhang, X.; You, J. Large Cation Ethylammonium Incorporated Perovskite for Efficient and Spectra Stable Blue Light-Emitting Diodes. *Nat. Commun.* **2020**, *11*, 4165.
- (23) Liu, Z.; Qiu, W.; Peng, X.; Sun, G.; Liu, X.; Liu, D.; Li, Z.; He, F.; Shen, C.; Gu, Q.; Ma, F.; Yip, H.-L.; Hou, L.; Qi, Z.; Su, S.-J. Perovskite Light-Emitting Diodes with EQE Exceeding 28% through a Synergetic Dual-Additive Strategy for Defect Passivation and Nanostructure Regulation. *Adv. Mater.* **2021**, *33*, 2103268.
- (24) Byun, J.; Cho, H.; Wolf, C.; Jang, M.; Sadhanala, A.; Friend, R. H.; Yang, H.; Lee, T.-W. Efficient Visible Quasi-2D Perovskite Light-Emitting Diodes. *Adv. Mater.* **2016**, *28*, 7515–7520.
- (25) Mitzi, D. B.; Wang, S.; Feild, C. A.; Chess, C. A.; Guloy, A. M. Conducting Layered Organic-Inorganic Halides Containing < 110>-Oriented Perovskite Sheets. *Science* **1995**, *267*, 1473–1476.
- (26) Ubrig, N.; Ponomarev, E.; Zultak, J.; Domaretskiy, D.; Zólyomi, V.; Terry, D.; Howarth, J.; Gutiérrez-Lezama, I.; Zhukov, A.; Kudrynskyi, Z. R.; Kovalyuk, Z. D.; Patané, A.; Taniguchi, T.; Watanabe, K.; Gorbachev, R. V.; Fal'ko, V. I.; Morpurgo, A. F. Design of Van Der Waals Interfaces for Broad-Spectrum Optoelectronics. *Nat. Mater.* **2020**, *19*, 299–304.
- (27) Wen, Y.; He, P.; Yao, Y.; Zhang, Y.; Cheng, R.; Yin, L.; Li, N.; Li, J.; Wang, J.; Wang, Z.; Liu, C.; Fang, X.; Jiang, C.; Wei, Z.; He, J. Bridging the Van Der Waals Interface for Advanced Optoelectronic Devices. *Adv. Mater.* **2020**, *32*, 1906874.
- (28) Cao, J.; Jing, X.; Yan, J.; Hu, C.; Chen, R.; Yin, J.; Li, J.; Zheng, N. Identifying the Molecular Structures of Intermediates for Optimizing the Fabrication of High-Quality Perovskite Films. *J. Am. Chem. Soc.* **2016**, *138*, 9919–9926.
- (29) Chen, S.; Dai, X.; Xu, S.; Jiao, H.; Zhao, L.; Huang, J. Stabilizing Perovskite-Substrate Interfaces for High-Performance Perovskite Modules. *Science* **2021**, *373*, 902.
- (30) Wang, J.; Luo, S.; Lin, Y.; Chen, Y.; Deng, Y.; Li, Z.; Meng, K.; Chen, G.; Huang, T.; Xiao, S.; Huang, H.; Zhou, C.; Ding, L.; He, J.; Huang, J.; Yuan, Y. Templated Growth of Oriented Layered Hybrid Perovskites on 3D-Like Perovskites. *Nat. Commun.* **2020**, *11*, 582.
- (31) Yin, W.; Li, M.; Dong, W.; Luo, Z.; Li, Y.; Qian, J.; Zhang, J.; Zhang, W.; Zhang, Y.; Kershaw, S. V.; Zhang, X.; Zheng, W.; Rogach, A. L. Multidentate Ligand Polyethylenimine Enables Bright Color-Saturated Blue Light-Emitting Diodes Based on CsPbBr<sub>3</sub> Nano-platelets. *ACS Energy Lett.* **2021**, *6*, 477–484.
- (32) Chen, B.; Chen, H.; Hou, Y.; Xu, J.; Teale, S.; Bertens, K.; Chen, H.; Proppe, A.; Zhou, Q.; Yu, D.; Xu, K.; Vafaei, M.; Liu, Y.; Dong, Y.; Jung, E. H.; Zheng, C.; Zhu, T.; Ning, Z.; Sargent, E. H. Passivation of the Buried Interface via Preferential Crystallization of 2D Perovskite on Metal Oxide Transport Layers. *Adv. Mater.* **2021**, *33*, 2103394.
- (33) Kong, L.; Zhang, X.; Li, Y.; Wang, H.; Jiang, Y.; Wang, S.; You, M.; Zhang, C.; Zhang, T.; Kershaw, S. V.; Zheng, W.; Yang, Y.; Lin, Q.; Yuan, M.; Rogach, A. L.; Yang, X. Smoothing the Energy Transfer Pathway in Quasi-2D Perovskite Films Using Methanesulfonate Leads to Highly Efficient Light-Emitting Devices. *Nat. Commun.* **2021**, *12*, 1246.
- (34) Yu, M.; Yi, C.; Wang, N.; Zhang, L.; Zou, R.; Tong, Y.; Chen, H.; Cao, Y.; He, Y.; Wang, Y.; Xu, M.; Liu, Y.; Jin, Y.; Huang, W.; Wang, J. Control of Barrier Width in Perovskite Multiple Quantum Wells for High Performance Green Light-Emitting Diodes. *Adv. Opt. Mater.* **2019**, *7*, 1801575.
- (35) Xiao, Z.; Kerner, R. A.; Zhao, L.; Tran, N. L.; Lee, K. M.; Koh, T.-W.; Scholes, G. D.; Rand, B. P. Efficient Perovskite Light-Emitting Diodes Featuring Nanometre-Sized Crystallites. *Nat. Photonics* **2017**, *11*, 108–115.
- (36) Xing, J.; Zhao, Y.; Askerka, M.; Quan, L. N.; Gong, X.; Zhao, W.; Zhao, J.; Tan, H.; Long, G.; Gao, L.; Yang, Z.; Voznyy, O.; Tang, J.; Lu, Z.-H.; Xiong, Q.; Sargent, E. H. Color-Stable Highly Luminescent Sky-Blue Perovskite Light-Emitting Diodes. *Nat. Commun.* **2018**, *9*, 3541.
- (37) Zhang, X.; Bai, X.; Wu, H.; Zhang, X.; Sun, C.; Zhang, Y.; Zhang, W.; Zheng, W.; Yu, W. W.; Rogach, A. L. Water-Assisted Size and Shape Control of CsPbBr<sub>3</sub> Perovskite Nanocrystals. *Angew. Chem., Int. Ed.* **2018**, *57*, 3337–3342.
- (38) Gao, W.; Zielinski, K.; Drury, B. N.; Carl, A. D.; Grimm, R. L. Elucidation of Chemical Species and Reactivity at Methylammonium Lead Iodide and Cesium Tin Bromide Perovskite Surfaces via Orthogonal Reaction Chemistry. *J. Phys. Chem. C* **2018**, *122*, 17882–17894.
- (39) Kharlamova, M. V.; Kramberger, C.; Rudatis, P.; Pichler, T.; Eder, D. Revealing the Doping Effect of Encapsulated Lead Halogenides on Single-Walled Carbon Nanotubes. *Appl. Phys. A: Mater. Sci. Process.* **2019**, *125*, 320.
- (40) Ju, D.; Kim, D.; Yook, H.; Han, J. W.; Cho, K. Controlling Electrostatic Interaction in PEDOT:PSS to Overcome Thermoelectric Tradeoff Relation. *Adv. Funct. Mater.* **2019**, *29*, 1905590.
- (41) Zeng, M.; Wang, X.; Ma, R.; Zhu, W.; Li, Y.; Chen, Z.; Zhou, J.; Li, W.; Liu, T.; He, Z.; Yan, H.; Huang, F.; Cao, Y. Dopamine Semiquinone Radical Doped PEDOT:PSS: Enhanced Conductivity, Work Function and Performance in Organic Solar Cells. *Adv. Energy Mater.* **2020**, *10*, 2000743.
- (42) Woo, S.; Kim, J. S.; Lee, T.-W. Characterization of Stability and Challenges to Improve Lifetime in Perovskite LEDs. *Nat. Photonics* **2021**, *15*, 630–634.
- (43) Guo, Y.; Apergi, S.; Li, N.; Chen, M.; Yin, C.; Yuan, Z.; Gao, F.; Xie, F.; Brocks, G.; Tao, S.; Zhao, N. Phenylalkylammonium Passivation Enables Perovskite Light Emitting Diodes with Record High-Radiance Operational Lifetime: The Chain Length Matters. *Nat. Commun.* **2021**, *12*, 644.
- (44) Miao, Y.; Ke, Y.; Wang, N.; Zou, W.; Xu, M.; Cao, Y.; Sun, Y.; Yang, R.; Wang, Y.; Tong, Y.; Xu, W.; Zhang, L.; Li, R.; Li, J.; He, H.; Jin, Y.; Gao, F.; Huang, W.; Wang, J. Stable and Bright Formamidinium-Based Perovskite Light-Emitting Diodes with High Energy Conversion Efficiency. *Nat. Commun.* **2019**, *10*, 3624.
- (45) Wang, H.; Kosasih, F. U.; Yu, H.; Zheng, G.; Zhang, J.; Pozina, G.; Liu, Y.; Bao, C.; Hu, Z.; Liu, X.; Kobera, L.; Abbrent, S.; Brus, J.;

Jin, Y.; Fahlman, M.; Friend, R. H.; Ducati, C.; Liu, X.-K.; Gao, F. Perovskite-Molecule Composite Thin Films for Efficient and Stable Light-Emitting Diodes. *Nat. Commun.* **2020**, *11*, 891.

(46) Wang, H.; Zhang, X.; Wu, Q.; Cao, F.; Yang, D.; Shang, Y.; Ning, Z.; Zhang, W.; Zheng, W.; Yan, Y.; Kershaw, S. V.; Zhang, L.; Rogach, A. L.; Yang, X. Trifluoroacetate Induced Small-Grained  $\text{CsPbBr}_3$  Perovskite Films Result in Efficient and Stable Light-Emitting Devices. *Nat. Commun.* **2019**, *10*, 665.

(47) Zhu, S.; Meng, Q.; Wang, L.; Zhang, J.; Song, Y.; Jin, H.; Zhang, K.; Sun, H.; Wang, H.; Yang, B. Highly Photoluminescent Carbon Dots for Multicolor Patterning, Sensors, and Bioimaging. *Angew. Chem., Int. Ed.* **2013**, *52*, 3953–3957.

(48) Jeong, S.-H.; Park, J.; Han, T.-H.; Zhang, F.; Zhu, K.; Kim, J. S.; Park, M.-H.; Reese, M. O.; Yoo, S.; Lee, T.-W. Characterizing the Efficiency of Perovskite Solar Cells and Light-Emitting Diodes. *Joule* **2020**, *4*, 1206–1235.